Topological description of the Stone-Wales defect formation energy in carbon nanotubes and graphene

Elif Ertekin* and D. C. Chrzan
Department of Materials Science and Engineering, University of California, Berkeley, California 94720, USA and Materials Sciences Division, Lawrence Berkeley National Laboratory, Berkeley, California 94720, USA

Murray S. Daw
Department of Physics and Astronomy, Clemson University, Clemson, South Carolina 29634, USA
(Received 4 February 2009; published 15 April 2009)

We develop a topological continuum framework to compute the formation energies of Stone-Wales defects in graphene and carbon nanotubes. Our approach makes no *a priori* assumptions about the analytical form of the dislocation strain fields while explicitly accounting for boundary conditions and defect-defect interactions. The continuum formalism reproduces trends observed in the atomistic simulations remarkably well and demonstrates the necessity of considering long-ranged effects to accurately describe defect energetics in graphene-based systems.

DOI: 10.1103/PhysRevB.79.155421 PACS number(s): 61.46.−w

I. INTRODUCTION

Recent glimpses into the nature of carbon nanotube deformation under tensile loading at high temperature indicate that the formation and motion of topological defects are critical components of nanoscale plasticity in these systems. Elongations of nanotubes up to 280% (in conjunction with diameter reduction) at high temperatures have been observed accompanied by the presence of kinklike structures in the graphene network.[1] This plasticity is related to the movement of topological defects (analogous to dislocations in bulk materials) which traverse the graphene network via carbon adatom diffusion, vacancy diffusion, and in particular glide and climblike processes, thus allowing for nanotube elongation that maintains a near-perfect hexagonal network.[2–6] High resolution transmission electron microscopy (TEM) images of topological defects in nanotubes in the vicinity of the kinks now provide the first direct evidence of defect-mediated plasticity.[7]

One particular defect in graphene [Fig. 1(a)], known as the Stone-Wales (SW) defect [Figs. 1(b) and 1(c)], has long been expected to play a large role in the plastic deformation of carbon nanotubes.[2–4,8–18] These defects are analogous to dislocation dipoles in bulk materials and are liable to form and dissociate, upon which the consistent dislocations may glide or climb through the lattice in response to externally applied loads.[8–12] [Dissociated SW defects are illustrated in Figs. 1(d) and 1(e).] Also, the dissociation of SW defects in carbon nanotubes induces a change in chirality, resulting in changes to the electronic structure.[11] Many authors have proposed exploiting this feature to create nanotube heterojunctions and other devices.[19–22]

If such mechanisms of plasticity are operational in carbon nanotubes, they can have important consequences for nanomechanical systems incorporating carbon nanotube components such as, e.g., torsional shafts,[23,24] torsional springs,[25] etc. Then, it will be important to develop a complete description of plastic deformation in carbon nanotubes and to understand how SW defects form and interact with each other. In the literature one can find many atomic scale investigations of the formation energy of the SW defect, both in carbon nanotubes[8,10,12,14–16,18,26] as well as graphene.[8,10,12,16,18,26] The reported values for SW defect formation energies both in carbon nanotubes and graphene[8,10,12,14–16,18,26] vary substantially: from around 5 (Ref. 10) to 6.3 eV (Ref. 18) in graphene and from around 3 (Ref. 15) to 5.5 eV (Ref. 27) in carbon nanotubes. These discrepancies may in part arise from differences in boundary conditions and defect interactions.

In nanotubes, it has long been appreciated that defect formation energies depend largely on the nanotube radius, the orientation of the dislocation dipole, and, to a lesser extent, the chirality.[10,15,16] But in addition to curvature effects, there is another contribution to differences in formation energies: the dislocation nature of SW defects. Dislocations have long-ranged stress fields, resulting in dislocation-dislocation interactions and a large dependence of the formation energy on the imposed boundary conditions and the periodicity of the defect arrangement.[28–32] We demonstrate here that this effect must be explicitly accounted for, as it can result in large variations in defect formation energies.

In Ref. 33, we presented a generalized continuum formalism to compute formation energies of SW [Figs. 1(b) and 1(c)] and dissociated SW [Figs. 1(d) and 1(e)] defects in graphene layers and carbon nanotubes. This formalism is a straightforward transferable continuum description that accurately predicts defect formation energies as compared with first-principles results. Here, we detail our continuum approach further: we develop a framework that naturally accommodates the effect of long-ranged interactions between defects while accurately predict dislocation formation energies in graphene and carbon nanotubes for a variety of geometries, system sizes, and defect-defect interactions. We demonstrate that large variations to defect formation energies can result solely from long-ranged interactions and differences in boundary conditions, highlighting the importance and necessity of accounting for these effects in continuum models.

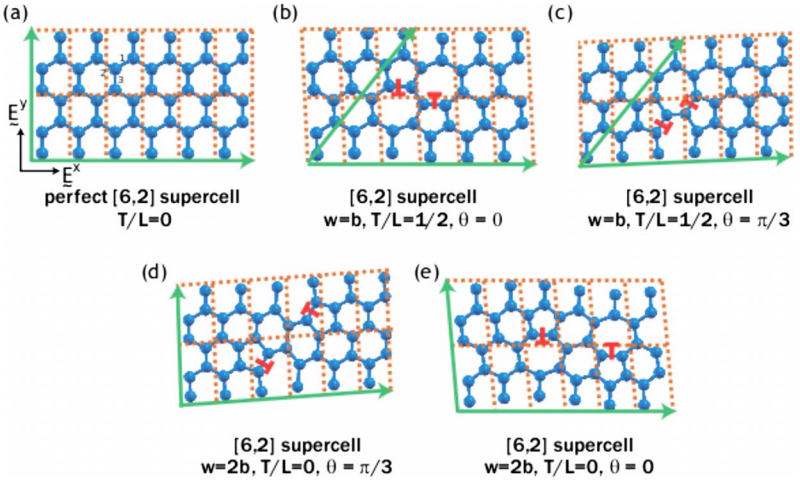

FIG. 1. (Color online) Illustration of various $[m,n]=[6,2]$ supercells with dipoles of varying orientation angle ϕ, dipole separation w, and stacking offset T/L.

Our formalism can account for out-of-plane buckling which results in local changes to the curvature that can screen out the dislocation strain fields (for a discussion of buckling in membranes, see Ref. 34). It is different from previous continuum formulations of SW defect formation in carbon nanotubes and graphene[15,35] because it makes no *a priori* assumptions about the nature of the dislocation strain fields but is derived from the fundamental topological constraints imposed by the dislocations present and naturally accounts for boundary conditions and defect interactions. It is a self-contained continuum approach which removes the need to introduce artificial "membrane thicknesses" that are often employed. By comparing the results of the continuum analysis to first-principles results for a variety of defect geometries, we extract an estimate for the dislocation core radius.

Additionally, graphene-based systems provide one of few examples in which continuum models can be directly compared to atomistic simulation. Most bulk or three-dimensional systems are too large for systematic atomistic simulations to assess the validity of continuum models, even though these continuum models are implemented in dislocation dynamics simulations to understand deformation and plasticity. By applying our approach to graphene and carbon nanotubes and comparing the results to those obtained from first principles, we demonstrate the remarkable capacity of a continuum formalism to capture real trends (provided that the continuum formalism correctly accounts for long-ranged interactions).

Thus, using our approach, the formation energies of dislocation defects in graphene and nanotubes can be accurately predicted without resorting to expensive atomistic calculations. This enables the development of statistical mechanics tools to study effects such as nanoplasticity and the brittle-ductile transition in nanotube and other graphene-based systems.

II. THEORETICAL BACKGROUND: GEOMETRY AND ATOMISTIC APPROACH

For the atomistic calculations, total energy electronic structure methods are employed in this study. We use density functional theory, invoking the local density approximation to the exchange-correlation potential as implemented in the *Vienna Ab Initio Simulation Package*.[36,37] Ultrasoft Vanderbilt pseudopotentials[38] are used in conjunction with a plane-wave basis set with cutoff energy of 211 eV. All results reported are converged to the number of significant figures given, both with respect to plane-wave cutoff and k-point sampling (chosen via a Monkhorst-Pack scheme).

A. Graphene layers

Graphene supercells are constructed for a variety of defect densities and defect orientations as illustrated in Fig. 1. We first create an $[m,n]$ graphene supercell containing a defect (m and n are integers that describe the number of cells present along the $\underset{\sim}{E}^x$ and $\underset{\sim}{E}^y$ directions, respectively; for instance, Fig. 1 illustrates defects in the $[6, 2]$ supercell). The total area is then $\Omega_A=(ma_1)(na_2)$, where $a_1=\sqrt{3}a$ and $a_2=3a$ are the side lengths of the subunits in Fig. 1 and $a\approx 1.42$ Å is the carbon-carbon spacing in graphene. The Burgers vector of the dislocations comprising the SW defect has magnitude $b=\sqrt{3}a$. As illustrated in Figs. 1 and 2, a variety of supercells can be created by varying the orientation angle ϕ of the dislocation dipole and the dipole separation w (we consider two possibilities: $w=b$ for a SW defect; $w=2b$ for a dissociated defect). Periodic boundary conditions are implemented in the first-principles calculations, resulting

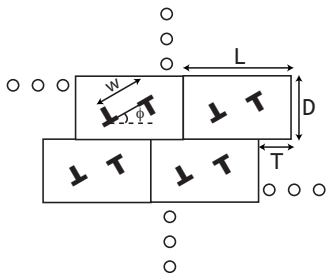

FIG. 2. The stacking procedure implemented in the atomistic calculations for graphene sheets. Stacking offsets of $T/L=0$ and $T/L=1/2$ and orientation angles of $\phi=0$ and $\phi=\pi/3$ are considered. Dipole separations of $w=b$ and $w=2b$ are considered.

TABLE I. Stone-Wales ($w=b$) defect formation energies in graphene for various supercell sizes $[m,n]$, supercell offsets $T/L=0$ and $T/L=1/2$, and orientation angles $\phi=0$ and $\phi=\pi/3$. E_a, accurate to within ± 0.05 eV, represents the formation energies determined *ab initio* and E_c represents the formation energies determined via continuum theory using core radius $r_c=0.96$ Å.

$[m,n]$	T/L	w	ϕ	E_a (eV)	E_c (eV)
[4,2]	0	b	0	4.21	3.90
	1/2	b	0	4.71	4.59
	0	b	$\pi/3$	5.45	5.12
	1/2	b	$\pi/3$	4.81	4.59
[4,4]	0	b	0	4.28	4.25
	1/2	b	0	4.27	4.25
	0	b	$\pi/3$	5.69	5.26
	1/2	b	$\pi/3$	5.71	5.25
[4,6]	0	b	0	4.21	4.25
	0	b	$\pi/3$	5.90	5.39
	1/2	b	$\pi/3$	5.90	5.39
[6,2]	0	b	0	4.33	4.05
	1/2	b	0	4.98	5.33
	0	b	$\pi/3$	5.40	5.36
	1/2	b	$\pi/3$	4.33	4.60
[6,4]	0	b	0	4.57	4.75
	1/2	b	0	4.60	4.83
	0	b	$\pi/3$	5.23	5.19
	1/2	b	$\pi/3$	5.17	5.14
[8,2]	0	b	0	4.35	4.05
	1/2	b	0	4.89	5.34
	0	b	$\pi/3$	5.44	5.50
	1/2	b	$\pi/3$	4.56	4.78
[8,4]	0	b	0	4.63	4.87
	1/2	b	0	4.74	5.09
	0	b	$\pi/3$	5.16	5.21
	1/2	b	$\pi/3$	4.95	5.09
[8,6]	0	b	0	4.68	4.97
	0	b	$\pi/3$	5.21	5.22
[10,2]	0	b	0	4.35	4.05
	0	b	$\pi/3$	5.47	5.58
[10,4]	0	b	0	4.65	4.90
	0	b	$\pi/3$	5.14	5.24
[12,2]	0	b	0	4.35	4.05
	0	b	$\pi/3$	5.51	5.64
[12,4]	0	b	0	4.65	4.91
	0	b	$\pi/3$	5.20	5.26

TABLE II. Dissociated ($w=2b$) defect formation energies in graphene for various supercell sizes $[m,n]$, supercell offsets $T/L=0$ and $T/L=1/2$, and orientation angles $\phi=0$ and $\phi=\pi/3$. E_a, accurate to within ± 0.05 eV, represents the formation energies determined *ab initio* and E_c represents the formation energies determined via continuum theory using core radius $r_c=09.6$ Å.

$[m,n]$	T/L	w	ϕ	E_a (eV)	E_c (eV)
[4,2]	0	$2b$	0	6.16	6.04
	1/2	$2b$	0	7.63	7.41
	0	$2b$	$\pi/3$	10.73	10.58
	1/2	$2b$	$\pi/3$	7.73	7.41
[4,4]	0	$2b$	0	6.70	6.72
	1/2	$2b$	0	6.66	6.74
	0	$2b$	$\pi/3$	11.65	10.59
	1/2	$2b$	$\pi/3$	11.60	10.55
[4,6]	0	$2b$	0	6.59	6.73
	0	$2b$	$\pi/3$	12.81	11.13
	1/2	$2b$	$\pi/3$	12.76	11.13
[6,2]	0	$2b$	0	7.13	6.98
	1/2	$2b$	0	10.52	10.82
	0	$2b$	$\pi/3$	11.48	11.78
	1/2	$2b$	$\pi/3$	7.46	8.31
[6,4]	0	$2b$	0	8.66	8.96
	1/2	$2b$	0	8.83	9.21
	0	$2b$	$\pi/3$	10.99	10.67
	1/2	$2b$	$\pi/3$	10.68	10.39
[8,2]	0	$2b$	0	7.29	7.02
	1/2	$2b$	0	10.64	11.31
	0	$2b$	$\pi/3$	11.79	12.34
	1/2	$2b$	$\pi/3$	8.56	9.29
[8,4]	0	$2b$	0	9.16	9.51
	1/2	$2b$	0	9.79	10.25
	0	$2b$	$\pi/3$	10.85	10.82
	1/2	$2b$	$\pi/3$	10.02	10.25
[8,6]	0	$2b$	0	9.37	9.85
	0	$2b$	$\pi/3$	10.96	10.83
[10,2]	0	$2b$	0	7.38	7.03
	0	$2b$	$\pi/3$	11.99	12.67
[10,4]	0	$2b$	0	9.30	9.64
	0	$2b$	$\pi/3$	10.88	10.96
[12,2]	0	$2b$	0	7.37	7.03
	0	$2b$	$\pi/3$	12.20	12.89
[12,4]	0	$2b$	0	9.34	9.67
	0	$2b$	$\pi/3$	10.99	11.06

in a variety of stacking mechanisms for the supercells, as illustrated in Fig. 2. We have considered stacking offsets of $T/L=0$ and $T/L=1/2$.

Historically, atomistic studies of dislocation dipoles in three-dimensional crystals with periodic boundary conditions have presented "lattice mismatch" problems at the supercell boundaries.[28] The lattice vectors of the perfect supercell are not the natural lattice vectors that capture the translational periodicity of the dislocated supercell. Typically, when dislocation dipoles are introduced into an otherwise perfect supercell, the lattice vectors of the perfect supercell are sheared to the lattice vectors of the defected lattice (e.g., see Refs. 28, 30, and 33). To a first approximation, the appropriate shear is given by[28]

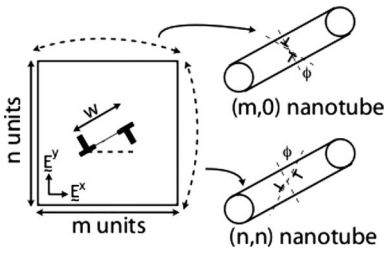

FIG. 3. The wrapping procedure used to construct zigzag and armchair carbon nanotubes with dislocation defects from planar graphene sheets. The defects considered are again SW defects ($w=b$) and dissociated SW defects ($w=2b$). Note that the definition of the angle ϕ in carbon nanotubes is different from how it is defined in graphene sheets.

$$m\underset{\sim}{a}_1 \rightarrow m(\underset{\sim}{a}_1 + \Delta\underset{\sim}{a}_1) = m\left[\underset{\sim}{a}_1 + \frac{w\sin\phi}{\sqrt{3}n}(\cos\phi\underset{\sim}{E}^x + \sin\phi\underset{\sim}{E}^y)\right], \tag{1}$$

$$n\underset{\sim}{a}_2 \rightarrow n(\underset{\sim}{a}_2 + \Delta\underset{\sim}{a}_2) \tag{2}$$

$$= n\left[\underset{\sim}{a}_2 - \frac{w\cos\phi}{m}(\cos\phi\underset{\sim}{E}^x + \sin\phi\underset{\sim}{E}^y)\right]. \tag{3}$$

These shears are incorporated in the defective supercells shown in Fig. 1.

We also note here that there is a degeneracy in the definition of the orientation angle ϕ for SW defects in graphene. The two pentagon-heptagon pairs which constitute the two dislocations in the dipole can be chosen in two different manners. For instance, the SW defect shown in Fig. 1(b) is illustrated with an orientation angle $\phi=0$ but can also be described by $\phi=\pi/3$. To avoid ambiguity, we always define ϕ so that it gives the minimum value of the continuum energy E_c (described in Sec. II B). In Fig. 1(b), because the choice of $\phi=0$ results in the formation of tilt boundaries, it is the minimum energy description of the system. For the SW defect in Fig. 1(c), we can choose either $\phi=\pi/3$ or $\phi=2\pi/3$; in this particular case the continuum energy is the same for either description. [For the atomistic studies, once an orientation ϕ is selected, the lattice vectors are sheared appropriately according to Eq. (1).]

In this study, we have used a total of 74 different stacking configurations for defects in graphene layers; the results are summarized in Tables I and II for SW and dissociated defects, respectively. The atomistic formation energies E_a are defined as the difference between a perfect $[m,n]$ supercell and one containing a dislocation dipole and properly sheared according to Eq. (1). The graphene sheets remain flat upon defect introduction, indicating that they are metastable to buckling.

B. Carbon nanotubes

The procedure used to construct defected nanotubes is given in Fig. 3. A defect is introduced into a graphene supercell, and before the shear in Eq. (1) is incorporated, the layer is then wrapped into a cylinder. By wrapping so that the $\underset{\sim}{E}^y$ axis becomes the nanotube axis, a zigzag nanotube of chirality $(m,0)$ with a defect present every n units along its axis is created. By wrapping so that the $\underset{\sim}{E}^x$ axis becomes the nanotube axis, an armchair nanotube of chirality (n,n) results, now with a defect occurring every m units along its axis. In addition to zigzag and armchair nanotubes constructed in this manner, we have also considered a chiral (12,3) nanotube in this study. The orientation angle ϕ is redefined for carbon nanotubes so that it represents the angle of the dislocation dipole measured from a cut of the nanotube normal to its axis, as illustrated in Fig. 3.

In analogy with Eq. (1) for graphene, the nanotube should be "sheared" to its natural state upon dislocation introduction in the atomistic calculations. This "shear" corresponds to introducing a twist and/or a shear along the axis of the nanotubes, depending on the dipole orientation. Ideally the dislocated nanotubes should be twisted and sheared accordingly, but doing so disrupts the axial periodicity of the supercell which must be maintained for our first-principles calculations. The periodicity could be maintained by using a sufficiently long tube, but the computational cost for the large number of atoms is too large for the resources available to us. Therefore, we do not shear the dislocated nanotubes to their natural state and the computed energy difference E_t between a perfect and a defected tube consists of two components:

$$E_t = E_a + E_s, \tag{4}$$

where E_a is the natural defect formation energy and E_s is the elastic energy present due to the suppression of shear. In a linear theory, the two energies can be directly superposed because there is no cross term between the internal dislocation strain and the external strain which shears the dislocated nanotube from its natural state.[39] This linear approximation is valid when the defect core remains largely unaffected by the applied external load; it is expected to breakdown with larger applied loads that can change the structure of the core.

For the shears associated with Eq. (1), the elastic energy E_s is

$$E_s = \frac{1}{2}c^{z\theta z\theta}\left[b\frac{w}{(ma_1)(na_2)}\right]^2\Omega_A, \tag{5}$$

where $c^{z\theta z\theta}$ is the shear modulus for graphene (measured as energy per unit area). We have, for a few select cases, computed the defect formation energy in a nanotube at its natural state; for these, Eqs. (4) and (5) hold, as expected, indicating that we are considering regimes where the applied loads are not large enough to substantially distort the defect core. Therefore the linear superposition is accurate.

A total of 47 carbon nanotubes has been investigated in this study. Most of these are zigzag and armchair tubes constructed in the manner indicated in Fig. 3, although we have also looked at a chiral (12,3) carbon nanotube. The first-principles formation energies E_t, E_s, and E_a of SW defects and dissociated SW defects are given in Tables III–V. Comparing Tables I–V, one can see that the defect formation energy E_a in a carbon nanotube constructed from an under-

TABLE III. Stone-Wales ($w=b$) defect formation energies E_a from *ab initio*, accurate to ± 0.05 eV, for armchair and zigzag carbon nanotubes of varying radii. The underlying supercell refers to the planar graphene structure that is wrapped according to Fig. 3 to generate the nanotube. For comparison, the energies E_c for optimized parameters $r_c=0.97$ Å and $c_g=3$ eV are provided.

Chirality	Supercell	w	ϕ radians	E_t (eV)	E_s (eV)	E_a (eV)	E_c (eV)
(8,0)	[8,2]	b	0	3.90	0.93	2.97	2.48
(10,0)	[10,2]	b	0	4.00	0.75	3.25	2.79
(12,0)	[12,2]	b	0	4.04	0.62	3.42	3.00
(20,0)	[20,2]	b	0	4.09	0.37	3.72	3.46
Graphene	$[\infty,2]$	b	0				≈4.4
(10,0)	[10,4]	b	0	3.50	0.37	3.13	3.09
(12,0)	[12,4]	b	0	3.65	0.31	3.34	3.32
(20,0)	[20,4]	b	0	4.03	0.19	3.84	3.82
Graphene	$[\infty,4]$	b	0				≈4.6
(6,6)	[4,6]	b	$\pi/2$	3.40	0.62	2.78	2.73
(10,10)	[4,10]	b	$\pi/2$	3.76	0.37	3.39	3.36
Graphene	$[4,\infty]$	b	0				≈4.3
(6,6)	[8,6]	b	$\pi/2$	3.28	0.31	2.97	2.88
(10,10)	[8,10]	b	$\pi/2$	3.81	0.19	3.62	3.60
Graphene	$[8,\infty]$	b	0				≈4.7
(10,0)	[10,2]	b	$\pi/3$	3.94	0.75	3.19	3.44
(12,0)	[12,2]	b	$\pi/3$	4.22	0.62	3.59	3.79
(20,0)	[20,2]	b	$\pi/3$	4.84	0.37	4.46	4.59
(10,0)	[10,4]	b	$\pi/3$	3.25	0.37	2.88	3.05
(12,0)	[12,4]	b	$\pi/3$	3.54	0.31	3.23	3.36
(20,0)	[20,4]	b	$\pi/3$	4.11	0.19	3.92	4.02
(6,6)	[4,6]	b	$\pi/6$	4.57	0.62	3.95	3.40
(10,10)	[4,10]	b	$\pi/6$	4.51	0.37	4.14	4.15
(6,6)	[8,6]	b	$\pi/6$	3.60	0.31	3.29	3.23
(10,10)	[8,10]	b	$\pi/6$	4.12	0.19	3.93	3.88

lying $[m,n]$ supercell is lower than that of the corresponding planar $[m,n]$ graphene sheet, as expected. However, the formation energy increases with increasing nanotube radius. As the radius of the nanotube $\rightarrow\infty$, buckling becomes less effective for relieving local stresses, and the formation energy E_a approaches that of the defect in a sheet of graphene, although the convergence is slow.

III. THEORETICAL BACKGROUND: CONTINUUM APPROACH

We now generalize the continuum approach presented by Daw[32] to the computation of dislocation formation energies in graphene layers and carbon nanotubes. The basic premise of our theory is simple and can be summarized as follows: the elastic distortion field resulting from a defect configuration is that which minimizes the total energy but is consistent with the topological constraints imposed by the defects. We use this premise to solve for the distortion fields and energy of a given defect configuration. Our approach can be applied to any two-dimensional surface embedded in a three-dimensional space. The basic differential geometry formalism and notation that are adopted here are described in Refs. 40 and 41. Vectors and covectors are both denoted with a tilde underneath, while second-order tensors are denoted in boldface.

We denote by $[\underset{\sim}{u}]_{\mathcal{B}_o}=u_i\underset{\sim}{E}^i$ the displacement field that results when topological defects are introduced into an otherwise perfect two-dimensional system. In this notation, the brackets and the subscripts in $[\cdot]_{\mathcal{B}_o}$ are used to indicate the coordinate system in which the components of the enclosed tensor are expressed, and $\underset{\sim}{E}^i$ denotes the coordinate basis. Associated with this displacement field are local elastic strains and changes to the local principal curvatures of the surface. The total energy associated with a deforming surface is expressed by

$$E_c=\frac{1}{2}\int c^{ijkl}\Delta_{ij}\Delta_{kl}dA+\frac{1}{2}c_g\int(\kappa_1\kappa_2)dA+\frac{1}{2}c_m\int(\kappa_1+\kappa_2)^2dA. \quad (6)$$

In Eq. (6), the first term consists of the elastic strain energy

TABLE IV. Dissociated Stone-Wales ($w=2b$) defect formation energies E_a from *ab initio*, accurate to ± 0.05 eV, for armchair and zigzag carbon nanotubes of varying radii. The underlying supercell refers to the planar graphene structure that is wrapped according to Fig. 3 to generate the nanotube. For comparison, the energies E_c for optimized parameters $r_c=0.97$ Å and $c_g=3$ eV are provided.

Chirality	Supercell	w	ϕ radians	E_t (eV)	E_s (eV)	E_a (eV)	E_c (eV)
(10,0)	[10,2]	$2b$	0	5.75	2.98	3.77	3.64
(12,0)	[12,2]	$2b$	0	6.62	2.49	4.13	4.17
(20,0)	[20,2]	$2b$	0	6.73	1.49	5.24	5.41
Graphene	[∞,2]	$2b$	0				≈7.8
(10,0)	[10,4]	$2b$	0	5.87	1.49	4.38	4.27
(12,0)	[12,4]	$2b$	0	5.88	1.24	4.64	4.84
(20,0)	[20,4]	$2b$	0	6.69	0.75	5.94	6.29
Graphene	[∞,4]	$2b$	0				≈9.3
(6,6)	[4,6]	$2b$	$\pi/2$	6.75	2.49	4.26	3.99
(10,10)	[4,10]	$2b$	$\pi/2$	6.69	1.49	5.20	5.12
Graphene	[4,∞]	$2b$	0				≈6.7
(6,6)	[8,6]	$2b$	$\pi/2$	6.23	1.24	4.99	4.72
(10,10)	[8,10]	$2b$	$\pi/2$	7.07	0.75	6.32	6.26
Graphene	[8,∞]	$2b$	0				≈9.5
(10,0)	[10,2]	$2b$	$\pi/3$	10.24	2.98	7.25	7.04
(12,0)	[12,2]	$2b$	$\pi/3$	10.68	2.49	8.20	8.01
(20,0)	[20,2]	$2b$	$\pi/3$	11.63	1.49	10.14	10.26
(10,0)	[10,4]	$2b$	$\pi/3$	7.35	1.49	5.85	5.30
(12,0)	[12,4]	$2b$	$\pi/3$	7.75	1.24	6.51	6.02
(20,0)	[20,4]	$2b$	$\pi/3$	8.84	0.75	8.09	7.63
(6,6)	[4,6]	$2b$	$\pi/6$	7.37	2.49	4.88	5.49
(10,10)	[4,10]	$2b$	$\pi/6$	8.51	1.49	7.02	7.60
(6,6)	[8,6]	$2b$	$\pi/6$	6.33	1.24	5.09	5.15
(10,10)	[8,10]	$2b$	$\pi/6$	6.74	0.75	6.00	6.85

(there is an implied summation over repeated indices). The last two terms are the contributions of the bending energy, for which we have chosen a Helfrich form[42] in which the energy depends on the local Gaussian and mean curvatures. The distortion tensor $[\mathbf{\Delta}]_{\mathcal{B}_o}=\Delta_{ij}\underset{\sim}{E}^i\otimes\underset{\sim}{E}^j$, whose components we wish to determine by minimization of E_c, is defined by $\Delta_{ij}=u_{j;i}$ ($\otimes$ denotes the tensor product while $u_{j;i}$ is the covariant derivative of the j component of the displacement field in the i direction). κ_1 and κ_2 are the principal curvatures of the surface. c^{ijkl} are elastic constants of the graphene sheet, c_g is the Gaussian curvature (saddle-splay) constant, and c_m is the mean curvature (splay) constant.

TABLE V. Stone-Wales ($w=b$) and dissociated Stone-Wales ($w=2b$) defect formation energies E_a from *ab initio* for (12,3) carbon nanotubes with different bond rotations, accurate to ± 0.05 eV. For comparison, the energies E_c for optimized parameters $r_c=0.97$ Å and $c_g=3$ eV are provided. The bonds to which the Nos. 1–3 correspond are illustrated in Fig. 1(a).

w	Rotated bond	ϕ radians	E_t (eV)	E_s (eV)	E_a (eV)	E_c (eV)
b	1	10.9	3.69	0.35	3.34	3.45
b	2	70.9	3.79	0.35	3.44	3.46
b	3	10.9	3.68	0.35	3.32	3.45
$2b$	1	10.9	6.45	1.42	5.03	5.29
$2b$	2	49.1	8.67	1.42	6.93	7.18
$2b$	3	70.9	7.68	1.42	5.94	6.23

In general, the introduction of topological defects results in local changes to the curvatures κ_1 and κ_2. In the inextensible limit (corresponding to $c^{ijkl}\to\infty$), the membrane responds to the introduction of defects by changing its curvature to screen out the strain fields completely. In this limit, the changes to the curvature are quantized in accordance with the Gauss-Bonnet theorem[43] for topological defects. We

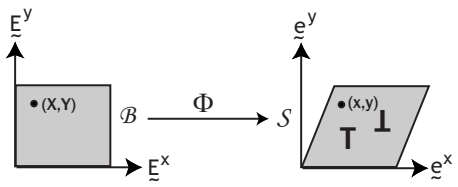

FIG. 4. Deformation map $\Phi:\mathcal{B}\to\mathcal{S}$ induced by the introduction of dislocations in an otherwise perfect graphene sheet.

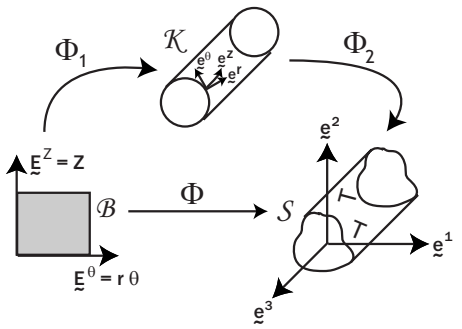

FIG. 5. Deformation map $\Phi:\mathcal{B}\rightarrow\mathcal{S}$ induced by the introduction of dislocations in an otherwise perfect carbon nanotube.

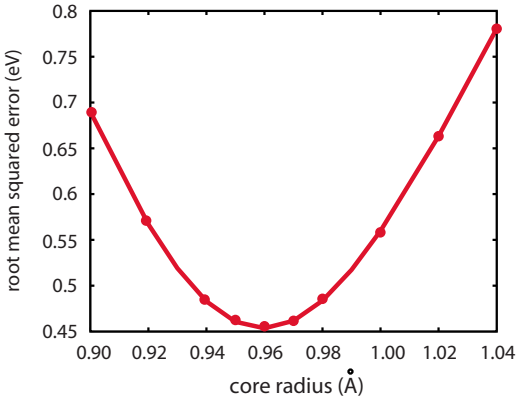

FIG. 6. (Color online) The root-mean-squared error for the continuum formalism for various values of the core radius $r_c \in [0.90, 1.04]$ Å in graphene. The error is minimized at $r_c = 0.96$ Å.

do not make this assumption here, instead we use the calculated elastic constants for graphene and allow both for local strains as well as bending. Thus, the expression for the total energy includes a Helfrich contribution[42] for the bending energy which has been used in descriptions of bending in lipid membranes and amphiphilic films comprised of liquid crystals. Conventional stability theory for these films assumes that the surface has a preferred (reference) curvature. Deviations from that preferred curvature result in an energy penalty. Helfrich[42] demonstrated that the functional form for this energy penalty can be expanded in terms of the components of the curvature tensor for the surface. In the case that the energy penalty is an isotropic function of the curvature, it can be expressed in terms of the first and second invariants of the curvature tensor, namely, the trace (the mean curvature) and determinant (the Gaussian curvature). This approach is applicable to a range of elastic materials which can be modeled as very thin films; other authors have used this approach for graphene as well (see, for instance, Ref. 44). As stated there, the approach works best when the atomic interactions are short-ranged so that they act along the film.

The distortion field Δ associated with a given distribution of defects is that which minimizes the total energy E_c but is consistent with the topological constraints imposed by the defects. These constraints are expressed in the form of a dislocation density tensor $\underset{\sim}{\alpha}$, analogous to the Nye tensor,[32]

$$\alpha_m = \epsilon^{kl}\Delta_{lm;k} = \sum_{j=1}^{N_{\text{disl}}} b_m^j \delta(\underset{\sim}{X} - \underset{\sim}{X}_o^j), \tag{7}$$

where $\underset{\sim}{X}_o^j$ denotes the position of the jth dislocation, b_m^i denotes the m component of its Burgers vector, $\Delta_{lm;k}$ denotes the covariant derivative of Δ_{lm} in the k direction, and ϵ^{kl} is defined by $\epsilon^{11}=\epsilon^{22}=0$, $\epsilon^{12}=1$, and $\epsilon^{21}=-1$. Again, there is an implied summation over repeated indices in Eq. (7).

As noted by Daw,[32] the formalism presented above results in a sum for the elastic part of the energy E_c in Eq. (6) that is only conditionally convergent, owing to the singularity at the dislocation core in Eq. (7). Typically the convergence is rendered absolute by smearing the delta function so that Eq. (7) becomes a Gaussian,

$$\alpha_m = \epsilon^{kl}\Delta_{lm;k} = \sum_{j=1}^{N_{\text{disl}}} \frac{b_m^j}{\pi r_c^2} \exp\left(-\frac{(\underset{\sim}{r} - \underset{\sim}{r}_o^j)^2}{r_c^2}\right), \tag{8}$$

where r_c is the dislocation core radius, one of the two fitting parameters that will be used in our analysis (the other is the saddle-splay constant c_g). Note that in the limit $r_c \rightarrow 0$, Eq. (8) recovers the form of Eq. (7).

Our description of the distortion is based on covariant derivatives of displacement fields, which are defined on tangent surfaces of manifolds (related to deformation gradients). Because it is defined from the tangent surface rather than from manifold chords, the deformation gradient is not always sufficient to describe the local deformation, as described in Arroyo and Belytschko.[45] The description that we have adopted is accurate only if the deformation itself varies smoothly relative to the size of the basis vectors. Although deformation fields near the cores of defects are not smooth, we will introduce a core radius to smooth the singularities and serve as an adjustable parameter to correctly describe the strain energy in the defect core. The use of the deformation gradient is sufficient for accurate descriptions of defect energetics as long as the core radius serves as an effective "smearing parameter" to smooth the distortion near the core and accurately describe the strain energy contained in it. Additionally, the use of the Helfrich form[42] in Eq. (6) recaptures some of the details that are lost by the use of the deformation gradient; for instance, there is now an energy penalty associated with rolling a graphene sheet into a nanotube. Ultimately, of course, the validity of the approach and the resulting distortion tensor is provided by comparing results to those obtained from atomistic simulations.

A. Graphene layers

The reference configuration $\mathcal{B}$ corresponding to a defect-free flat graphene supercell (illustrated in Fig. 4) is a two-manifold. $\mathcal{B}$ is a logical choice for the reference configuration, as it is the defect-free, strain-free, and bend-free ground state of the graphene membrane. A given point $\underset{\sim}{X}$ in $\mathcal{B}$ is denoted with coordinates (X,Y) in the Cartesian basis $\mathcal{B}_o = (\underset{\sim}{E}^x, \underset{\sim}{E}^y)$ so that $\underset{\sim}{X} = X\underset{\sim}{E}^x + Y\underset{\sim}{E}^y$. Here, $X \in [0, 2L_x]$, $Y \in [0, 2L_y]$, where $2L_x$ and $2L_y$ are the unstrained lengths of

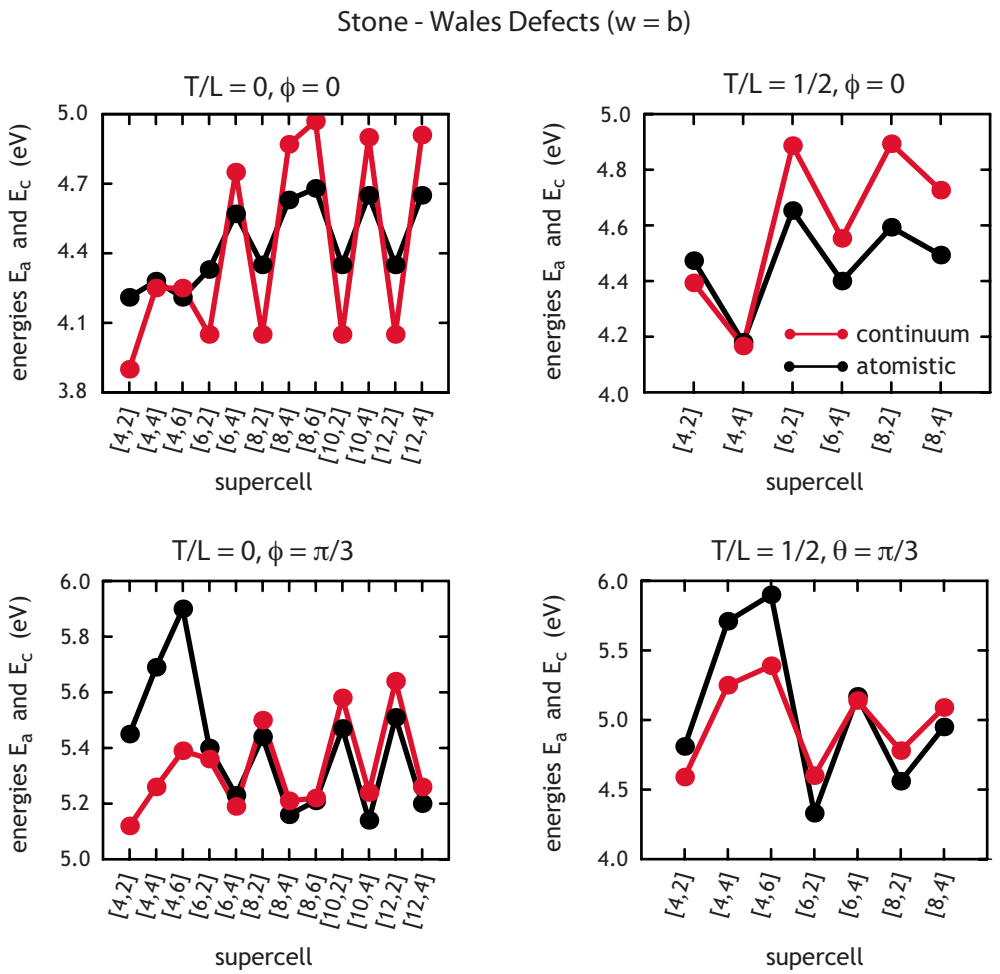

FIG. 7. (Color online) A direct comparison of the atomistic and continuum formation energies E_a and E_c, respectively, of SW defects in a variety of graphene supercells. The core radius of the dislocations is r_c=0.96 Å.

the graphene sheet along the directions $\underset{\sim}{E}^x$ and $\underset{\sim}{E}^y$, respectively. In the notation that follows, components and bases corresponding to the reference state $\mathcal{B}$ are indicated by capital letters. The dual basis $\mathcal{B}_o^*=(\underset{\sim}{E}_x,\underset{\sim}{E}_y)$ to $\mathcal{B}_o=(\underset{\sim}{E}^x,\underset{\sim}{E}^y)$ is defined by

$$\underset{\sim}{E}_i \cdot \underset{\sim}{E}^j = \delta_i^j. \tag{9}$$

Since $\mathcal{B}_o$ is a Cartesian basis, $\mathcal{B}_o=\mathcal{B}_o^*$.

We now deform the graphene supercell by introducing a distribution of dislocations. The resulting deformed state $\mathcal{S}$, also a two-manifold, is illustrated by the mapping $\Phi:\mathcal{B}\to\mathcal{S}$ as shown in Fig. 4. A given point $\underset{\sim}{x}=\Phi(\underset{\sim}{X})$ of $\mathcal{S}$ is described with coordinates $\underset{\sim}{x}=(x,y)$ in the Euclidean basis $\mathcal{S}_o=(\underset{\sim}{e}^x,\underset{\sim}{e}^y)$. (We denote components and bases corresponding to the deformed state $\mathcal{S}$ with lowercase letters.)

We write the deformation map Φ as

$$x = X + u_x,$$

$$y = Y + u_y, \tag{10}$$

where the displacement field (u_x,u_y) results directly from the dislocation defects.

For graphene sheets, the atomistic simulations did not buckle or exhibit changes to the curvature upon defect introduction, indicating that the graphene sheets are metastable to buckling upon defect introduction. Thus, we now concern ourselves only with the first (elastic term) in the expression for E_c. In this term, the implied summation is taken over the coordinates x and y. In this case, the covariant derivative $\Delta_{ij}=u_{j;i}$ is given simply by the derivative $u_{j,i}$, the derivative of the displacement field u_j in the i direction.

The two equations corresponding to the constraints in Eq. (7) are

$$\begin{aligned} m = x: \frac{\partial \Delta_{yx}}{\partial x} - \frac{\partial \Delta_{xx}}{\partial y} \\ = \sum_{j=1}^{N_{\text{disl}}} b_x^j \delta(\underset{\sim}{X} - \underset{\sim}{X}_o^j) \\ = \sum_{j=1}^{N_{\text{disl}}} b_x^j \delta(X - X_o^j)\delta(Y - Y_o^j), \end{aligned} \tag{11}$$

$$m = y:\frac{\partial \Delta_{yy}}{\partial x} - \frac{\partial \Delta_{xy}}{\partial y}$$
$$= \sum_{j=1}^{N_{\text{disl}}} b_y^j \delta(\underset{\sim}{X} - \underset{\sim}{X}_o^j)$$
$$= \sum_{j=1}^{N_{\text{disl}}} b_y^j \delta(X - X_o^j)\delta(Y - Y_o^j). \quad (12)$$

Now, the periodicity of the dislocation geometry allows us to write the distortion as a Fourier expansion,

$$\Delta_{ij}(\underset{\sim}{X}) = \sum_{\underset{\sim}{G}} \tilde{\Delta}_{ij}(\underset{\sim}{G})\exp[i\underset{\sim}{G}\cdot\underset{\sim}{X}], \quad (13)$$

where the sum is taken over reciprocal lattice vectors $\underset{\sim}{G} = G_x\underset{\sim}{E}^x + G_y\underset{\sim}{E}^y$,

$$G_x = \frac{\pi}{2L_xL_y}[p\underset{\sim}{a}_{2y} - q\underset{\sim}{a}_{1y}], \quad (14)$$

$$G_y = \frac{\pi}{2L_xL_y}[-p\underset{\sim}{a}_{2x} + q\underset{\sim}{a}_{1x}], \quad (15)$$

where p and q are integers indexing the reciprocal lattice vectors, $G = |\underset{\sim}{G}|$, and $\underset{\sim}{a}_{1x}$ denotes the $\underset{\sim}{E}^x$ component of $\underset{\sim}{a}_1$, etc. We can now write E_c as

$$E_c = \frac{1}{2}\int c^{ijkl}\Delta_{ij}\Delta_{kl}dA = \frac{\Omega_A}{2}\sum_{\underset{\sim}{G}} c^{ijkl}\tilde{\Delta}_{ij}\tilde{\Delta}_{kl}^*, \quad (16)$$

where * denotes the complex conjugate.

Using the Fourier expansion in the constraints of Eqs. (11) and (12) gives

$$m = x:i(G_x\tilde{\Delta}_{yx} - G_y\tilde{\Delta}_{xx}) = \sum_j^{N_{\text{disl}}} \frac{b_x^j}{4L_xL_y}\exp[-i\underset{\sim}{G}\cdot\underset{\sim}{X}_o^i], \quad (17)$$

$$m = y:i(G_x\tilde{\Delta}_{yy} - G_y\tilde{\Delta}_{xy}) = \sum_j^{N_{\text{disl}}} \frac{b_y^j}{4L_xL_y}\exp[-i\underset{\sim}{G}\cdot\underset{\sim}{X}_o^i]. \quad (18)$$

The solution to Eqs. (17) and (18) for the distortion field consists of inhomogeneous and homogeneous parts,

$$\tilde{\Delta}_{ij} = \tilde{\Delta}_{ij}^{\text{inh}} + \tilde{\Delta}_{ij}^{\text{hom}}. \quad (19)$$

The inhomogeneous solution satisfies the constraints imposed by the dislocations and can be expressed by

$$\tilde{\Delta}_{xx}^{\text{inh}} = \sum_j^{N_{\text{disl}}} \frac{ib_x^j}{\Omega_A}\frac{G_y}{G^2}\exp[-i\underset{\sim}{G}\cdot\underset{\sim}{X}_o^j], \quad (20)$$

$$\tilde{\Delta}_{yx}^{\text{inh}} = -\sum_j^{N_{\text{disl}}} \frac{ib_x^j}{\Omega_A}\frac{G_x}{G^2}\exp[-i\underset{\sim}{G}\cdot\underset{\sim}{X}_o^j], \quad (21)$$

$$\tilde{\Delta}_{xy}^{\text{inh}} = \sum_j^{N_{\text{disl}}} \frac{ib_y^j}{\Omega_A}\frac{G_y}{G^2}\exp[-i\underset{\sim}{G}\cdot\underset{\sim}{X}_o^j], \quad (22)$$

$$\tilde{\Delta}_{yy}^{\text{inh}} - \sum_j^{N_{\text{disl}}} \frac{ib_y^j}{\Omega_A}\frac{G_x}{G^2}\exp[-i\underset{\sim}{G}\cdot\underset{\sim}{X}_o^j]. \quad (23)$$

When the dislocation cores are smeared as in Eq. (8), the inhomogeneous solutions above [as well as the Fourier expansions in Eqs. (17) and (18)] are modified by a factor $\exp[-G^2r_c^2/4]\text{erf}(2L_x/r_c)\text{erf}(2L_y/r_c)$.

The homogeneous solution is superposed to the inhomogeneous solution so as to minimize the energy E_c in Eq. (16). Each term in the summation can be minimized independently of the others. The homogeneous solution can be written as

$$\tilde{\Delta}_{ij} = G_i\tilde{\chi}_j. \quad (24)$$

The vector $\tilde{\underset{\sim}{\chi}}(\underset{\sim}{G})$ is determined by minimizing each term in the summation in Eq. (16).

B. Carbon nanotubes

A primary difference between carbon nanotubes and graphene sheets is that when defects are introduced, the displacement field $\underset{\sim}{u}$ is no longer contained within the surface of the perfect tube. The nanotube surface is unstable to buckling, or deformation out of the surface, which can relieve strains, but at the cost of changing the curvature. Therefore, the full expression in Eq. (6) must now be utilized in the computation of E_c.

The reference configuration $\mathcal{B}$ (illustrated in Fig. 5) is again a two-manifold corresponding to a flat defect-free graphene supercell. A given point $\underset{\sim}{X}$ in $\mathcal{B}$ is denoted with coordinates $\underset{\sim}{X} = (X_\theta, X_z) = (r\theta, z)$ in the Euclidean basis $\mathcal{B}_o = (\underset{\sim}{E}^\theta, \underset{\sim}{E}^z)$ [the dual space to $\mathcal{B}_o = (\underset{\sim}{E}^\theta, \underset{\sim}{E}^z)$ is again denoted by $\mathcal{B}_o^* = (\underset{\sim}{E}_\theta, \underset{\sim}{E}_z)$]. Here, $z \in [0, 2L]$, $\theta \in [0, 2\pi]$, and $2\pi r$ and $2L$ are the unstrained lengths of the graphene sheet along the directions $\underset{\sim}{E}^\theta$ and $\underset{\sim}{E}^z$, respectively. The area of the nanotube supercell is $\Omega_A = (2\pi r)(2L)$.

We now deform the membrane as follows. First, in step $\Phi_1:\mathcal{B}\to\mathcal{K}$, we roll the sheet into a cylinder so that the $\underset{\sim}{E}_z$ direction is parallel to the cylinder axis. The cylindrical coordinate system $\mathcal{K}_o = (\underset{\sim}{e}_r, \underset{\sim}{e}_\theta, \underset{\sim}{e}_z)$ is defined on the perfect nanotube $\mathcal{K}$. Then, in step $\Phi_2:\mathcal{K}\to\mathcal{S}$, we introduce a distribution of dislocations. The resulting deformed state $\mathcal{S}$, also a two-manifold, is illustrated by the mapping $\Phi_2\circ\Phi_1 = \Phi:\mathcal{B}\to\mathcal{S}$ as shown in Fig. 5. A given point $\underset{\sim}{x} = \Phi(\underset{\sim}{X})$ of $\mathcal{S}$ is described with coordinates (x_1, x_2, x_3) in the Cartesian basis $\mathcal{S}_o = (\underset{\sim}{e}^1, \underset{\sim}{e}^2, \underset{\sim}{e}^3)$.

We write the deformation map Φ as

$$x_1 = r\cos\theta + u_r\cos\theta - u_\theta\sin\theta,$$
$$x_2 = r\sin\theta + u_r\sin\theta + u_\theta\cos\theta,$$
$$x_3 = z + u_z, \quad (25)$$

where the displacement field components $\underset{\sim}{u} = u_r\underset{\sim}{e}^r + u_\theta\underset{\sim}{e}^\theta + u_z\underset{\sim}{e}^z$ result directly from the dislocation defects (choosing $\underset{\sim}{u} = 0$ corresponds to a defect-free cylinder).

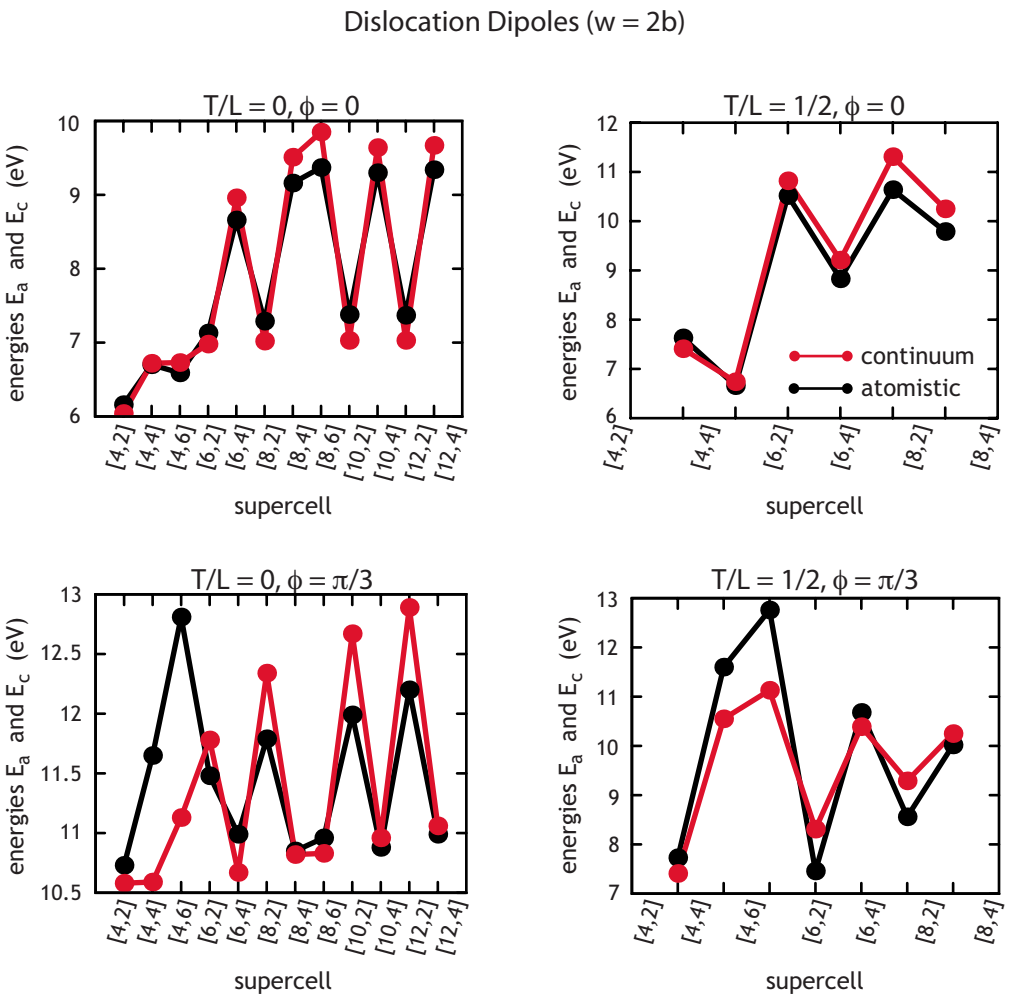

FIG. 8. (Color online) A direct comparison of the atomistic and continuum formation energies E_a and E_c, respectively, of dissociated defects in a variety of graphene supercells. The core radius of the dislocations is $r_c=0.96$ Å.

The relevant components of the distortion tensor Δ are given by the covariant derivatives of the field (u_r,u_θ,u_z) with respect to the $\underset{\sim}{e}^\theta$ and $\underset{\sim}{e}^z$ directions. They are given by

$$\Delta_{\theta\theta}=\frac{1}{r}\frac{\partial u_\theta}{\partial\theta}+\frac{u_r}{r},$$

$$\Delta_{z\theta}=\frac{\partial u_\theta}{\partial Z},$$

$$\Delta_{\theta z}=\frac{1}{r}\frac{\partial u_z}{\partial\theta},$$

$$\Delta_{zz}=\frac{\partial u_z}{\partial Z},$$

$$\Delta_{\theta r}=\frac{1}{r}\frac{\partial u_r}{\partial\theta}-\frac{u_\theta}{r},$$

$$\Delta_{zr}=\frac{\partial u_r}{\partial Z}. \tag{26}$$

In the first term of Eq. (6), the implied summation is only taken over the indices (θ,z), as the local stretching associated with $\Delta_{\theta r}$ and Δ_{zr} does not contribute to the strain energy in a linear elastic theory.

The components of the distortion tensor $\Delta_{\theta r}$ and Δ_{zr} do however appear in the expression for the mean and Gaussian curvature of the deforming surface. In addition to straining the reference configuration, the deformation Φ introduces changes to the local principle curvatures κ_1 and κ_2. These can be described via the first and second fundamental forms, $[\mathbf{g}]_{\mathcal{S}_c}=g_{ij}\underset{\sim}{g}^i\otimes\underset{\sim}{g}^j$ and $[\mathbf{b}]_{\mathcal{S}_c}=b_{ij}\underset{\sim}{g}^i\otimes\underset{\sim}{g}^j$, respectively, for the deformed surface $\mathcal{S}$.

$\mathcal{S}_c=(\underset{\sim}{g}^\theta,\underset{\sim}{g}^z)$ denotes the *convected* basis induced on the surface $\mathcal{S}$ by the transformation $\Phi:\mathcal{B}\rightarrow\mathcal{S}$. The dual space to $\mathcal{S}_c=(\underset{\sim}{g}^\theta,\underset{\sim}{g}^z)$ is $\mathcal{S}_c^*=(\underset{\sim}{g}_\theta,\underset{\sim}{g}_z)$ and is defined by

$$\underset{\sim}{g}_\theta=\frac{\partial}{\partial X_\theta}(x_1,x_2,x_3)=\frac{1}{r}\frac{\partial}{\partial\theta}(x_1,x_2,x_3), \tag{27}$$

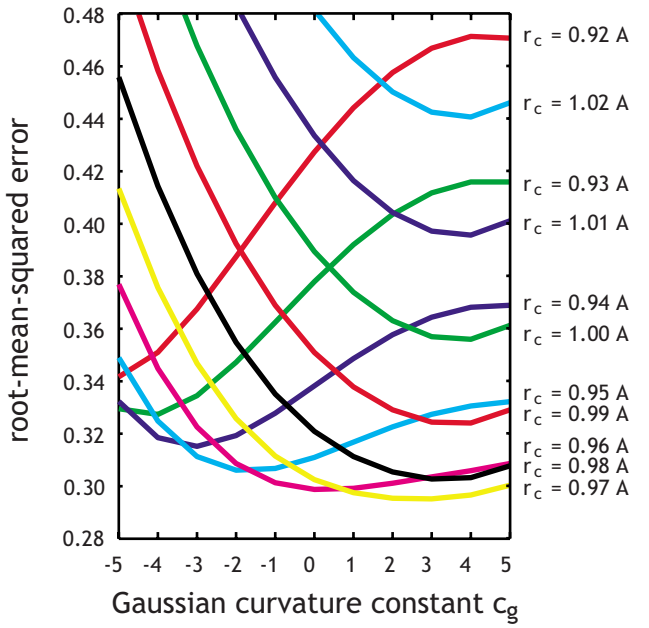

FIG. 9. (Color online) The root-mean-squared error between the continuum energies E_c and the atomistic energies E_a for various values of the core radius $r_c \in [0.90, 1.04]$ Å and saddle-splay constant $c_g \in [-5, 5]$ eV in carbon nanotubes. The error is minimized at $r_c = 0.97$ Å; $c_g = 3$ eV.

$$\underset{\sim}{g}_z = \frac{\partial}{\partial X_z}(x_1, x_2, x_3) = \frac{\partial}{\partial z}(x_1, x_2, x_3). \tag{28}$$

In differential geometry terms, the basis vectors $\mathcal{S}_c^* = (\underset{\sim}{g}_\theta, \underset{\sim}{g}_z)$ are the *push forward* of the basis vectors $\mathcal{B}_o^* = (\underset{\sim}{E}_\theta, \underset{\sim}{E}_z)$ by the map Φ.

The components of the first fundamental form $[\mathbf{g}]$ are given by the metric tensor,

$$g_{ij} = \langle \underset{\sim}{g}_i, \underset{\sim}{g}_j \rangle. \tag{29}$$

The unit normal to the deformed surface is given by

$$\underset{\sim}{n} = \frac{\underset{\sim}{g}_\theta \times \underset{\sim}{g}_z}{\| \underset{\sim}{g}_\theta \times \underset{\sim}{g}_z \|}, \tag{30}$$

where $\times$ denotes a vector cross product and $\|\cdot\|$ is the magnitude. The components of $\mathbf{b}$ are given by the inner product

$$b_{ij} = \langle \underset{\sim}{g}_{i,j}, \underset{\sim}{n} \rangle, \tag{31}$$

where

$$\underset{\sim}{g}_{i,j} = \frac{\partial}{\partial X_j \partial X_i}(x_1, x_2, x_3). \tag{32}$$

The Gaussian curvature is given by

$$\kappa_1 \kappa_2 = \frac{\det \mathbf{b}}{\det \mathbf{g}}, \tag{33}$$

and the mean curvature is given by

$$\kappa_1 + \kappa_2 = \mathrm{tr}[\mathbf{g}^{-1}\mathbf{b}], \tag{34}$$

where det is the determinant, tr is the trace, and $[\cdot]^{-1}$ denotes the inverse. After tedious but straightforward algebra, it is possible to express both the Gaussian and mean curvature in terms of the distortion tensor $\mathbf{\Delta}$. Neglecting terms that are higher than second order in Δ_{ij},

$$\begin{aligned}\kappa_1\kappa_2 = &-\frac{1}{r}\left(\frac{\partial \Delta_{zr}}{\partial z}\right) + \frac{2}{r}\left(\frac{\partial \Delta_{zr}}{\partial z}\right)\Delta_{zz} - \frac{1}{r}\left(\frac{\partial \Delta_{zz}}{\partial z}\right)\Delta_{zr} \\ &+ \frac{1}{r}\left(\frac{\partial \Delta_{z\theta}}{\partial z}\right)\Delta_{\theta r} - \left(\frac{\partial \Delta_{\theta r}}{\partial z}\right)^2 + \frac{1}{r}\left(\frac{\partial \Delta_{zr}}{\partial z}\right)\left(\frac{\partial \Delta_{\theta r}}{\partial \theta}\right) \\ &+ \frac{1}{r}\left(\frac{\partial \Delta_{zr}}{\partial z}\right)\Delta_{\theta\theta},\end{aligned} \tag{35}$$

$$\begin{aligned}(\kappa_1 + \kappa_2)^2 = &\frac{1}{r^2} - \frac{\Delta_{zr}^2}{r^2} - \frac{2}{r}\left(\frac{\partial \Delta_{zr}}{\partial z}\right) + \left(\frac{\partial \Delta_{zr}}{\partial z}\right)^2 + \frac{4}{r}\left(\frac{\partial \Delta_{zr}}{\partial z}\right)\Delta_{zz} \\ &- \frac{2}{r}\left(\frac{\partial \Delta_{zz}}{\partial z}\right)\Delta_{zr} + \frac{2}{r^2}\left(\frac{\partial \Delta_{zr}}{\partial \theta}\right)\Delta_{z\theta} + \frac{2}{r^2}\Delta_{r\theta}\Delta_{\theta r} \\ &+ \frac{2}{r}\left(\frac{\partial \Delta_{z\theta}}{\partial z}\right)\Delta_{\theta r} - \frac{1}{r^2}\Delta_{\theta r}^2 + \frac{2}{r}\left(\frac{\partial \Delta_{\theta r}}{\partial z}\right)\Delta_{\theta r} \\ &- \frac{2}{r^2}\left(\frac{\partial \Delta_{\theta r}}{\partial \theta}\right) + \frac{2}{r}\left(\frac{\partial \Delta_{zr}}{\partial z}\right)\left(\frac{\partial \Delta_{\theta r}}{\partial \theta}\right) + \frac{1}{r^2}\left(\frac{\partial \Delta_{\theta r}}{\partial \theta}\right)^2 \\ &+ \frac{2}{r^2}\left(\frac{\partial \Delta_{zr}}{\partial \theta}\right)\Delta_{\theta z} + \frac{2}{r^2}\Delta_{z\theta}\Delta_{\theta z} - \frac{2}{r^2}\left(\frac{\partial \Delta_{\theta z}}{\partial \theta}\right)\Delta_{zr} \\ &- \frac{2}{r^2}\Delta_{\theta\theta} + \frac{2}{r}\left(\frac{\partial \Delta_{zr}}{\partial z}\right)\Delta_{\theta\theta} + \frac{6}{r^2}\left(\frac{\partial \Delta_{\theta r}}{\partial \theta}\right)\Delta_{\theta\theta} + \frac{3}{r^2}\Delta_{\theta\theta}^2 \\ &+ \frac{2}{r^2}\left(\frac{\partial \Delta_{\theta\theta}}{\partial \theta}\right)\Delta_{\theta r}.\end{aligned} \tag{36}$$

Substituting in Eqs. (35) and (36) into Eq. (6), we have $E_c = E_c(\Delta)$. We wish to minimize E_c with respect to the distortion Δ while satisfying the topological constraints given in Eq. (7). The three equations corresponding to Eq. (7) are

$$\begin{aligned}m = z: &\frac{1}{r}\frac{\partial \Delta_{zz}}{\partial \theta} - \frac{\partial \Delta_{\theta z}}{\partial z} \\ &= \sum_{j=1}^{N_{\mathrm{disl}}} b_z^j \delta(\underset{\sim}{X} - \underset{\sim}{X}_o^j) \\ &= \sum_{j=1}^{N_{\mathrm{disl}}} \frac{b_z^j}{r}\delta(\theta - \theta_o^j)\delta(z - z_o^j),\end{aligned} \tag{37}$$

$$\begin{aligned}m = \theta: &\frac{1}{r}\frac{\partial \Delta_{z\theta}}{\partial \theta} + \frac{\Delta_{zr}}{r} - \frac{\partial \Delta_{\theta\theta}}{\partial z} \\ &= \sum_{j=1}^{N_{\mathrm{disl}}} b_\theta^j \delta(\underset{\sim}{X} - \underset{\sim}{X}_o^j) \\ &= \sum_{j=1}^{N_{\mathrm{disl}}} \frac{b_\theta^j}{r}\delta(\theta - \theta_o^j)\delta(z - z_o^j),\end{aligned} \tag{38}$$

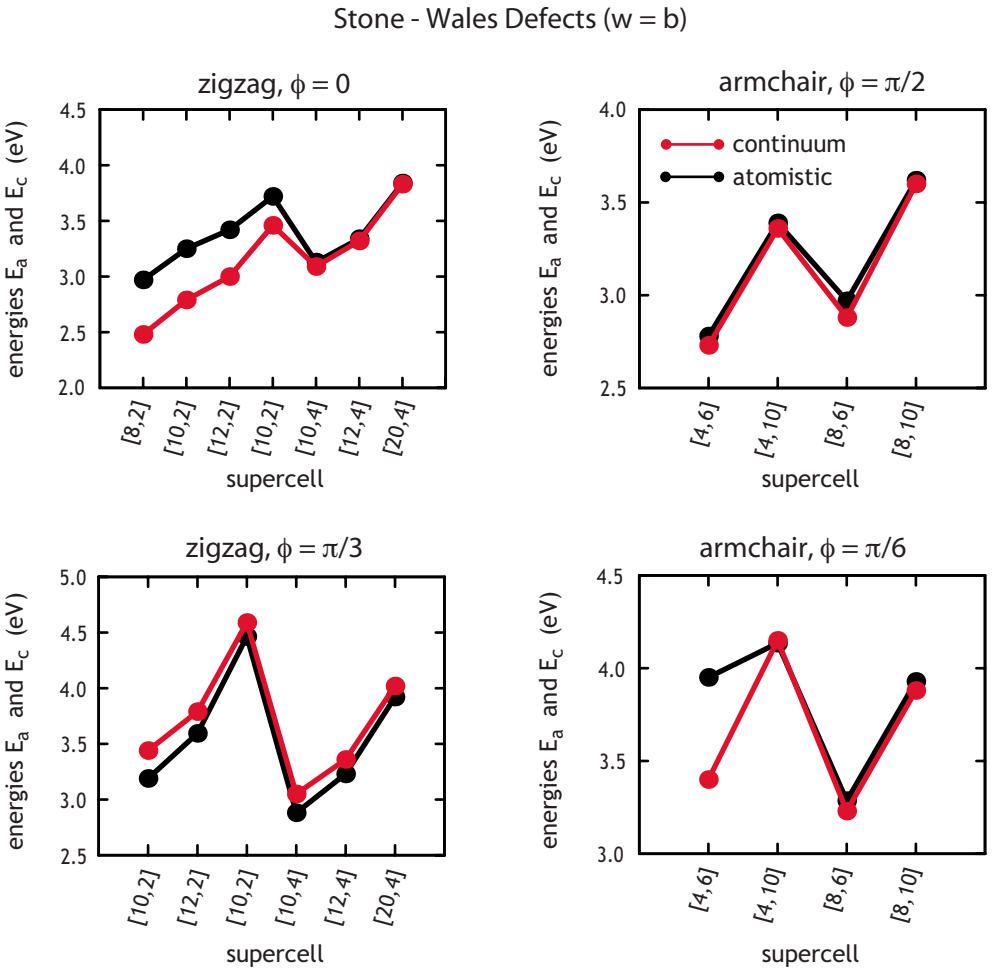

FIG. 10. (Color online) A direct comparison of the atomistic and continuum formation energies E_a and E_c, respectively, of Stone-Wales defects in a variety of armchair and zigzag carbon nanotubes. The core radius of the dislocations is r_c=0.97 Å and the saddle-splay constant is c_g=3 eV.

$$m = r:\frac{1}{r}\frac{\partial \Delta_{zr}}{\partial \theta} - \frac{\Delta_{z\theta}}{r} - \frac{\partial \Delta_{\theta r}}{\partial z}$$
$$= \sum_{j=1}^{N_{\text{disl}}} b_r^j \delta(\underset{\sim}{X} - \underset{\sim}{X}_o^j)$$
$$= \sum_{j=1}^{N_{\text{disl}}} \frac{b_r^j}{r}\delta(\theta - \theta_o^j)\delta(z - z_o^j). \quad (39)$$

Here, b_θ^j and b_z^j are the angular and axial components of the Burgers vector of the jth dislocation on the two-dimensional surface, but the quantity b_r^j simply denotes a jump in the mixed partial covariant derivatives of the displacement field u_r and does not correspond to a dislocation in the usual sense. To avoid introducing tears into the surface, we constrain b_r^j=0.

The periodicity of the dislocation geometry allows us to write the distortion as a Fourier expansion,

$$\Delta_{ij}(\underset{\sim}{X}) = \sum_{p,q} \tilde{\Delta}_{ij}(p,q)\exp[ip\theta]\exp\left[i\frac{q\pi}{L}z\right], \quad (40)$$

where the sum is taken over all integers p and q. Equations (37)–(39) now become

$$m = z:\frac{1}{r}(ip)\tilde{\Delta}_{zz} - i\left(\frac{q\pi}{L}\right)\tilde{\Delta}_{\theta z}$$
$$= \sum_{j}^{N_{\text{disl}}} \frac{b_z^j}{4\pi r L}\exp[-ip\theta_o^j]$$
$$\times\exp\left[-i\frac{q\pi}{L}z_o^j\right], \quad (41)$$

$$m = \theta:\frac{1}{r}(ip)\tilde{\Delta}_{z\theta} + \frac{1}{r}\tilde{\Delta}_{zr} - i\left(\frac{q\pi}{L}\right)\tilde{\Delta}_{\theta\theta}$$
$$= \sum_{j}^{N_{\text{disl}}} \frac{b_\theta^j}{4\pi r L}\exp[-ip\theta_o^j]$$
$$\times\exp\left[-i\frac{q\pi}{L}z_o^j\right], \quad (42)$$

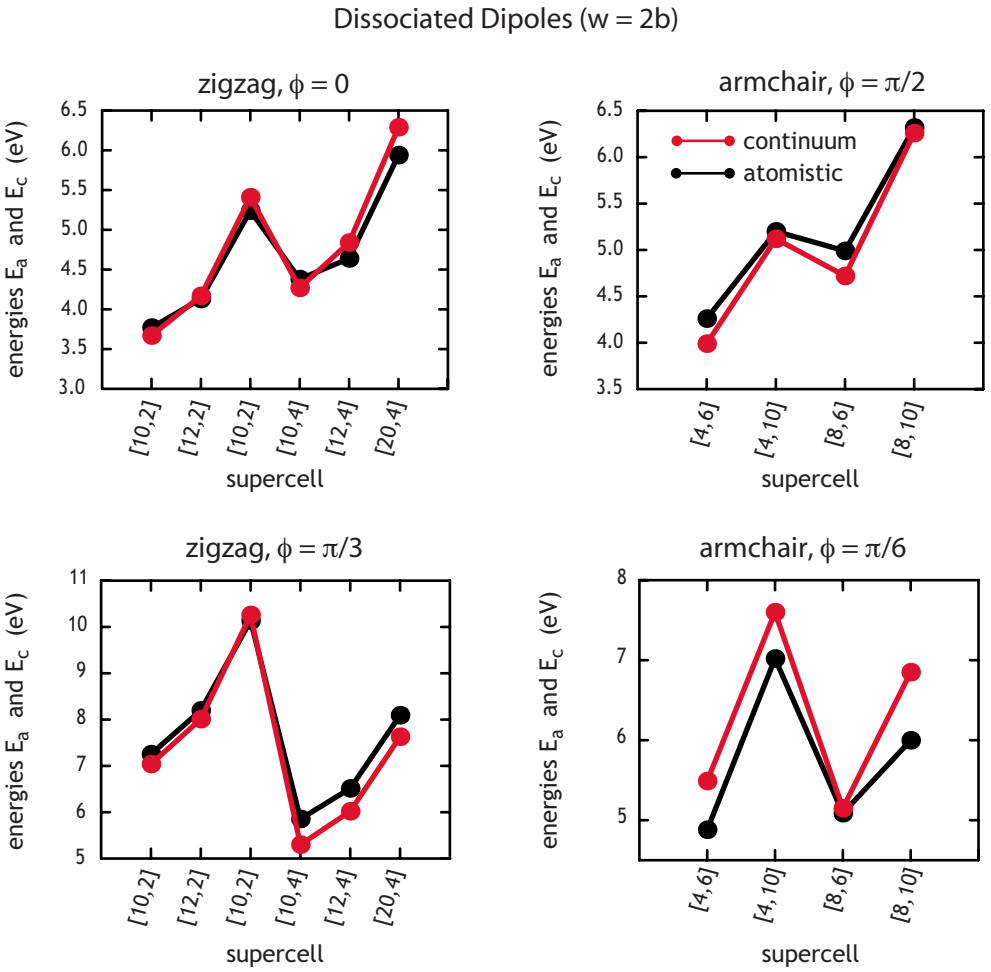

FIG. 11. (Color online) A direct comparison of the atomistic and continuum formation energies E_a and E_c, respectively, of dissociated defects in a variety of armchair and zigzag carbon nanotubes. The core radius of the dislocations is r_c=0.97 Å and the saddle-splay constant is c_g=3 eV.

$$m = r: \frac{1}{r}(ip)\tilde{\Delta}_{zr} - \frac{1}{r}\tilde{\Delta}_{z\theta} - i\left(\frac{q\pi}{L}\right)\tilde{\Delta}_{\theta r}$$
$$= \sum_{j}^{N_{\text{disl}}} \frac{b_r^j}{4\pi r L}\exp[-ip\theta_o^j]$$
$$\times \exp\left[-i\frac{q\pi}{L}z_o^j\right]. \quad (43)$$

As before, for each Fourier term, the solution to Eqs. (41)–(43) consists of inhomogeneous and homogeneous parts,

$$\tilde{\Delta}_{ij} = \tilde{\Delta}_{ij}^{\text{inh}} + \tilde{\Delta}_{ij}^{\text{hom}}. \quad (44)$$

The inhomogeneous solution satisfies the constraints imposed by the dislocations, while the homogeneous solution is chosen to minimize the total energy E_c in Eq. (6). Inserting Eq. (40) into Eq. (35), (36), and (6), one obtains

$$E_c = \frac{1}{2}\Omega_A \sum_{p,q} c^{ijkl}\tilde{\Delta}_{ji}\tilde{\Delta}_{lk}^* + \frac{1}{2}\Omega_A c_g \sum_{p,q}\left\{\frac{3i}{r}\left(\frac{q\pi}{L}\right)\tilde{\Delta}_{zr}\tilde{\Delta}_{zz}^* + \frac{i}{r}\left(\frac{q\pi}{L}\right)\tilde{\Delta}_{z\theta}\tilde{\Delta}_{\theta r}^* - \left(\frac{q\pi}{L}\right)^2\tilde{\Delta}_{\theta r}\tilde{\Delta}_{\theta r}^* + \frac{p}{r}\left(\frac{q\pi}{L}\right)\tilde{\Delta}_{zr}\tilde{\Delta}_{\theta r}^* + \frac{i}{r}\left(\frac{q\pi}{L}\right)\tilde{\Delta}_{zr}\tilde{\Delta}_{\theta\theta}^*\right\}$$
$$+ \frac{1}{2}\Omega_A c_m\left\{\frac{1}{r^2} + \sum_{p,q}\left[\left(\left(\frac{q\pi}{L}\right)^2 - \frac{1}{r^2}\right)\tilde{\Delta}_{zr}\tilde{\Delta}_{zr}^* + \left(\frac{p^2-1}{r^2} - \frac{2i}{r}\left(\frac{q\pi}{L}\right)\right)\tilde{\Delta}_{\theta r}\tilde{\Delta}_{\theta r}^* + \frac{3}{r^2}\tilde{\Delta}_{\theta\theta}\tilde{\Delta}_{\theta\theta}^* + \frac{6i}{r}\left(\frac{q\pi}{L}\right)\tilde{\Delta}_{zr}\tilde{\Delta}_{z\theta}^* + \frac{2}{r^2}\tilde{\Delta}_{r\theta}\tilde{\Delta}_{\theta r}^*\right.$$
$$\left. + \frac{4ip}{r^2}\tilde{\Delta}_{zr}\tilde{\Delta}_{\theta z}^* + \frac{2}{r^2}\tilde{\Delta}_{z\theta}\tilde{\Delta}_{\theta z}^* + \frac{4ip}{r^2}\tilde{\Delta}_{\theta r}\tilde{\Delta}_{\theta\theta}^* + \frac{2i}{r}\left(\frac{q\pi}{L}\right)\tilde{\Delta}_{zr}\tilde{\Delta}_{\theta\theta}^* + \frac{2p}{r}\left(\frac{q\pi}{L}\right)\tilde{\Delta}_{zr}\tilde{\Delta}_{\theta r}^*\right]\right\}. \quad (45)$$

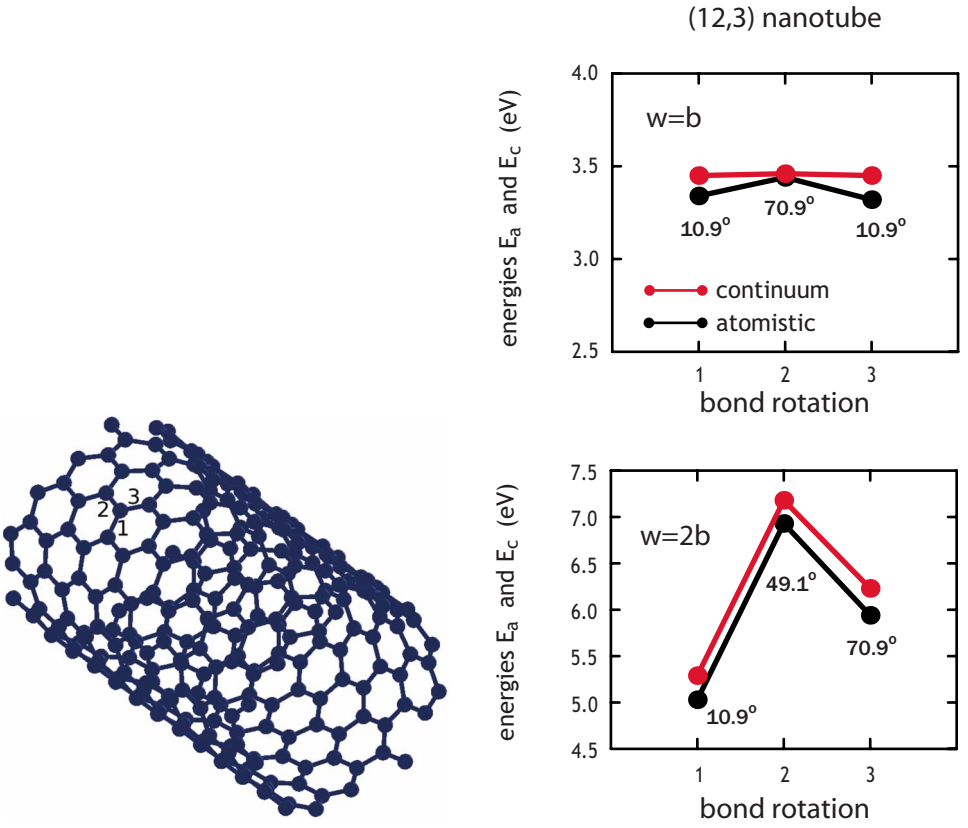

FIG. 12. (Color online) A direct comparison of the atomistic and continuum formation energies E_a and E_c, respectively, of Stone-Wales and dissociated Stone-Wales defects in (12,3) carbon nanotubes formed by rotating the bonds labeled 1–3. The core radius of the dislocations is r_c =0.97 Å and the saddle-splay constant is c_g=3 eV.

The first term is the elastic strain energy, the first term in braces is the Gaussian curvature, and the last term in braces is the mean curvature. Again, the energy arising from each Fourier term can be minimized independently of the others.

For each such term, an inhomogeneous solution to Eqs. (41)–(43) can be written as

$$\tilde{\Delta}_{zz}^{\mathrm{inh}} = \sum_j^{N_{\mathrm{disl}}} -\frac{i}{\Omega_A G^2}\left(\frac{p}{r}\right) b_z^j \exp\left[-i\left(p\theta_o^j + \frac{q\pi}{L} z_o^j\right)\right],$$

$$\tilde{\Delta}_{\theta z}^{\mathrm{inh}} = \sum_j^{N_{\mathrm{disl}}} \frac{i}{\Omega_A G^2}\left(\frac{q\pi}{L}\right) b_z^j \exp\left[-i\left(p\theta_o^j + \frac{q\pi}{L} z_o^j\right)\right],$$

$$\tilde{\Delta}_{\theta\theta}^{\mathrm{inh}} = \sum_j^{N_{\mathrm{disl}}} \frac{i}{\Omega_A G^2}\left(\frac{q\pi}{L}\right) b_\theta^j \exp\left[-i\left(p\theta_o^j + \frac{q\pi}{L} z_o^j\right)\right],$$

$$\tilde{\Delta}_{z\theta}^{\mathrm{inh}} = \sum_j^{N_{\mathrm{disl}}} -\frac{i}{\Omega_A G^2}\left(\frac{p}{r}\right) b_\theta^j \exp\left[-i\left(p\theta_o^j + \frac{q\pi}{L} z_o^j\right)\right],$$

$$\tilde{\Delta}_{\theta r}^{\mathrm{inh}} = \sum_j^{N_{\mathrm{disl}}} \frac{1}{\Omega_A G^2}\left(\frac{p}{r^2}\right)\left(\frac{q\pi}{L}\right) b_\theta^j \exp\left[-i\left(p\theta_o^j + \frac{q\pi}{L} z_o^j\right)\right],$$

$$\tilde{\Delta}_{zr}^{\mathrm{inh}} = 0, \tag{46}$$

where

$$G = \sqrt{\left(\frac{p}{r}\right)^2 + \left(\frac{q\pi}{L}\right)^2}. \tag{47}$$

As before, upon smearing the cores as described in Eq. (8), the inhomogeneous solutions above are modified by a factor $\exp[-G^2 r_c^2/4]\mathrm{erf}(2\pi r/r_c)\mathrm{erf}(2L/r_c)$.

Then, the homogeneous solution can be written in the form

$$\tilde{\Delta}_{zz}^{\mathrm{hom}} = \left(\frac{q\pi}{L}\right)\tilde{\chi}_z,$$

$$\tilde{\Delta}_{\theta z}^{\mathrm{hom}} = \left(\frac{p}{r}\right)\tilde{\chi}_z,$$

$$\tilde{\Delta}_{\theta\theta}^{\mathrm{hom}} = \left(\frac{p}{r}\right)\tilde{\chi}_\theta,$$

$$\tilde{\Delta}_{\theta r}^{\mathrm{hom}} = \left(\frac{p}{r}\right)\tilde{\chi}_r,$$

$$\tilde{\Delta}_{z\theta}^{\mathrm{hom}} = \begin{cases} -\dfrac{ip}{2}\left(\dfrac{q\pi}{L}\right)\tilde{\chi}_r, & |p| = 1 \\ \dfrac{p}{p^2-1}\left(\dfrac{q\pi}{L}\right)(p\tilde{\chi}_\theta + i\tilde{\chi}_r), & |p| \neq 1, \end{cases}$$

$$\tilde{\Delta}_{zr}^{\mathrm{hom}} = \begin{cases} \dfrac{p^2}{2}\left(\dfrac{q\pi}{L}\right)\tilde{\chi}_r, & |p| = 1 \\ \dfrac{p}{p^2-1}\left(\dfrac{q\pi}{L}\right)(p\tilde{\chi}_r - i\tilde{\chi}_\theta), & |p| \neq 1, \end{cases} \tag{48}$$

where the vector $\tilde{\chi}=(\tilde{\chi}_r,\tilde{\chi}_\theta,\tilde{\chi}_z)$ is determined by numerical minimization of the corresponding term in E_c.

C. Extensions and limitations of model

We believe that this approach can be extended to other types of topological defects such as disclinations. The basic premise should be similar: each defect presents a topological constraint on the distortion fields; the resulting distortion field is that which otherwise minimizes the energy. We are interested in using this theory to explore plasticity in graphenelike systems. However, this requires some tweaking of the model.

Defects can form in response to external loads in order to relieve local stresses. In such cases, defect formation energies are reduced. However, as with any linear continuum theory, there is no cross term or interaction between the defect and any applied external load, and therefore this effect cannot be captured directly in our approach. To account for this, one would need to adopt a nonlinear theory that captures changes in the defect core that might result from applied loads. Alternatively, within the framework of the model presented here, the change in defect formation energies can be represented by appropriate modifications to the core radius as a function of, say, the local stress. In this case, the nonlinear effects are then buried into changing the description of the defect core structure. Additionally, it is possible to adopt the approach typically employed in dislocation dynamics simulations in which changes to the core structure are ignored, but the external work done by applied loads to the defects is considered.

IV. RESULTS AND DISCUSSION

The elastic constants, isotropic for the graphene sheet, are determined from the *ab initio* results to be $c_{1111}=20.869$ eV/Å^2, $c_{1122}=3.794$ eV/Å^2, and $c_{1212}=c_{1221}=8.5374$ eV/Å^2. The mean curvature constant $c_m=0.729$ eV is determined by comparing the energies of perfect nanotubes to sheets of graphene.

A. Graphene layers

We considered core radii within the range $r_c \in [0.90, 1.04]$ Å in increments of 0.01 Å. In Fig. 6, the root-mean-squared error between E_a and E_c is plotted as a function of the core radius r_c for all of the graphene layers examined. This error is minimized at 0.454 eV when the core radius $r_c=0.96$ Å. Using this optimized value for the core radius, the average error is found to be 0.327 eV with a standard deviation of 0.317 eV.

In Figs. 7 and 8, a direct comparison between the atomistic results E_a and the continuum results E_c (with $r_c=0.96$ Å) is given for SW defects and dissociated dipoles, respectively. In both cases, the continuum results capture the patterns exhibited by the atomistic calculations remarkably well. Exact comparisons for each case are given in Tables I and II. For the SW defects, the root-mean-squared error is 0.261 eV and the average error is 0.217 eV with a standard deviation of 0.148 eV when the core radius is chosen to be 0.96 eV. For dissociated dipoles, with this selection of core radius, the root-mean-squared error is 0.586 eV, with an average error of 0.437 eV and standard deviation of 0.396 eV.

The plots in Figs. 7 and 8 exemplify the importance of understanding the role of the boundary conditions, defect-defect interactions, and defect orientation in determining the formation energy. These factors cause variations of the formation energies E_a of SW defects from 4.20 to 5.90 eV; the variation in E_a for dissociated dipoles (6.16–12.81 eV) is even more striking. These differences in energetics indicate that long-ranged interactions are prevalent in these systems and cannot be neglected in a proper continuum formalism.

The continuum results reproduce the first-principles trends very nicely, demonstrating that an accurate continuum formalism is applicable at this scale. The largest deviations occur in the smallest supercells (at high defect densities) when the dislocation cores may be more deformed. This may not be a problem for real systems since defect densities this high are unlikely to be observed. Additionally, the largest discrepancies appear for highly skew systems (i.e., $L_x \gg L_y$ or $L_y \gg L_x$). While it may be possible to improve the accuracy by using a nonlinear elasticity theory or further refining the definition of the core radius, the theory presented here may be sufficient for behavior that will be observed in real systems. Of course, it will need to be modified in any instance where a linear analysis is not sufficient. For instance, to determine the defect energetics when external loads are applied, a nonlinear approach may be necessary if the core structure is substantially altered. In this case, interaction effects might artificially be captured by appropriate modification of the core radius for applied loads, thus burying nonlinear effects into the description of the defect core.

B. Carbon nanotubes

In carbon nanotubes, the two fitting parameters are the dislocation core radius r_c and the Gaussian curvature constant c_g. Core radii within the range $r_c \in [0.90, 1.10]$ Å in increments of 0.01 Å and Gaussian curvature constants within the range $c_g \in [-5, 5]$ eV in increments of 1 eV were considered. The root-mean-squared error is plotted in Fig. 9; it is minimized around 0.295 eV at $r_c=0.97$ Å, $c_g=3$ eV. This corresponds well to the core radius of $r_c=0.96$ Å that was determined for graphene sheets in Sec. IV A. Our estimate of the saddle splay constant c_g obtained by minimizing the root-mean-squared error is different from that described in Ref. 44; however, we note from Fig. 9 that the rms error for $r_c=0.97$ Å is fairly flat across a range of values of c_g; using their value $c_g=-0.3$ eV will give nearly as a good a fit. Using our optimized parameters, the average magnitude of the error is 0.221 eV with a standard deviation of 0.198 eV. The root-mean-squared error in Stone-Wales defects is 0.226 eV; the average magnitude of the error is 0.159 eV

with a standard deviation of 0.164 eV. For the dissociated defects, the root-mean-squared error in dissociated Stone-Wales defects is 0.353 eV; the average magnitude of the error is 0.286 eV with a standard deviation of 0.212 eV.

To demonstrate that the continuum description with $r_c = 0.97$ Å, $c_g = 3$ eV captures well the trends exhibited in the atomistic analysis, Figs. 10 and 11 present a direct comparison of the atomistic energies E_a and the continuum energies E_c for Stone-Wales and dissociated Stone-Wales defects, respectively. These figures reflect the results obtained in the zigzag and armchair carbon nanotubes. Figure 12 shows a direct comparison of the results obtained in a chiral (12,3) nanotube for Stone-Wales and dissociated Stone-Wales defects. The different SW defect geometries are constructed by rotating one of the three distinct bonds (1, 2, and 3) in the (12,3) tube, labeled in the picture. Each rotation results in a specific orientation ϕ for the Stone-Wales or dissociated Stone-Wales defect in the nanotube, which is labeled on Fig. 12 and directly used in the continuum formalism. Again, the comparison is encouraging. Exact comparison of all results is provided in Tables III–V.

The ability of the continuum analysis to capture the trends is exemplified in Figs. 10–12. Overall, the trends between the atomistic and the continuum analysis compare remarkably well, indicating that the continuum description can be used to describe the properties of SW defects in carbon nanotubes while accounting for the long-range elastic fields explicitly. Once again, the variations in defect energetics show a large dependence on boundary conditions (2 eV variation for SW defects and as large as 6.5 eV variation for dissociated defects), illustrating the need to accommodate these effects in a proper formalism.

V. CONCLUSIONS

We present and implement a continuum model for computing the formation energies of Stone-Wales defects in graphene and carbon nanotubes. This model demonstrates the necessity and importance of correctly accounting for (1) the long-range interactions between these dislocationlike defects and (2) the boundary conditions for any relevant system. Defect energetics are shown to exhibit a large dependence on geometry, orientation, and system size. The comparison between atomistic and continuum results is good, directly demonstrating the remarkable ability of continuum analysis to capture real trends even at the nanoscale. Our approach provides a generalized framework and should be applicable to accurately and simply computing defect energetics in other systems as well. It can provide a mechanism for driving dislocation dynamics simulations or exploring ductile-brittle phase transitions in these systems.

ACKNOWLEDGMENTS

E.E. acknowledges the support of the Intel Corporation. This research was supported in part by the National Science Foundation under Contract No. DMR-0304629. The authors also acknowledge supercomputer time provided by the National Energy Research Scientific Computing Center.

*Corresponding author; elif@berkeley.edu

[1] J. Y. Huang, S. Chen, Z. Q. Wang, K. Kempa, Y. M. Wang, S. H. Jo, G. Chen, M. S. Dresselhaus, and Z. F. Ren, Nature (London) **439**, 281 (2006).
[2] J. Y. Huang, F. Ding, and B. I. Yakobson, Phys. Rev. Lett. **100**, 035503 (2008).
[3] F. Ding, K. Jiao, M. Wu, and B. I. Yakobson, Phys. Rev. Lett. **98**, 075503 (2007).
[4] F. Ding, K. Jiao, Y. Lin, and B. I. Yakobson, Nano Lett. **7**, 681 (2007).
[5] J. Y. Huang, S. Chen, Z. F. Ren, Z. Wang, K. Kempa, M. J. Naughton, G. Chen, and M. S. Dresselhaus, Phys. Rev. Lett. **98**, 185501 (2007).
[6] J. Y. Huang, S. Chen, Z. F. Ren, Z. Q. Wang, D. Z. Wang, M. Vaziri, Z. Suo, G. Chen, and M. S. Dresselhaus, Phys. Rev. Lett. **97**, 075501 (2006).
[7] K. Suenaga, H. Wakabayashi, M. Koshino, Y. Sato, K. Urita, and S. Iijima, Nat. Nanotechnol. **2**, 358 (2007).
[8] T. Dumitrica and B. I. Yakobson, Appl. Phys. Lett. **84**, 2775 (2004).
[9] T. Dumitrica, T. Belytschko, and B. I. Yakobson, J. Chem. Phys. **118**, 9485 (2003).
[10] G. Samsonidze, G. Samsonidze, and B. Yakobson, Comput. Mater. Sci. **23**, 62 (2002).
[11] B. I. Yakobson, Appl. Phys. Lett. **72**, 918 (1998).
[12] M. Buongiorno Nardelli, B. I. Yakobson, and J. Bernholc, Phys. Rev. B **57**, R4277 (1998).
[13] M. Buongiorno Nardelli, B. I. Yakobson, and J. Bernholc, Phys. Rev. Lett. **81**, 4656 (1998).
[14] P. Zhang, P. E. Lammert, and V. H. Crespi, Phys. Rev. Lett. **81**, 5346 (1998).
[15] H. Jiang, X.-Q. Feng, Y. Huang, K. Hwang, and P. Wu, Comput. Methods Appl. Mech. Eng. **193**, 3419 (2004).
[16] L. G. Zhou and S.-Q. Shi, Appl. Phys. Lett. **83**, 1222 (2003).
[17] K. Liew, X. He, and C. Wong, Acta Mater. **52**, 2521 (2004).
[18] Q. Zhao, M. Buongiorno Nardelli, and J. Bernholc, Phys. Rev. B **65**, 144105 (2002).
[19] P. Lambin, A. Fonseca, J. P. Vigneron, J. B. Nagy, and A. A. Lucas, Chem. Phys. Lett. **245**, 85 (1995).
[20] R. Saito, G. Dresselhaus, and M. S. Dresselhaus, Phys. Rev. B **53**, 2044 (1996).
[21] J.-C. Charlier, T. W. Ebbesen, and P. Lambin, Phys. Rev. B **53**, 11108 (1996).
[22] L. Chico, V. H. Crespi, L. X. Benedict, S. G. Louie, and M. L. Cohen, Phys. Rev. Lett. **76**, 971 (1996).
[23] A. M. Fennimore, T. D. Yuzvinsky, W.-Q. Han, M. S. Fuhrer, J. Cumings, and A. Zettl, Nature (London) **424**, 408 (2003).
[24] P. A. Williams, S. J. Papadakis, A. M. Patel, M. R. Falvo, S. Washburn, and R. Superfine, Phys. Rev. Lett. **89**, 255502 (2002).

[25] S. J. Papadakis, A. R. Hall, P. A. Williams, L. Vicci, M. R. Falvo, R. Superfine, and S. Washburn, Phys. Rev. Lett. **93**, 146101 (2004).
[26] P. Jensen, J. Gale, and X. Blase, Phys. Rev. B **66**, 193403 (2002).
[27] R. Conversano, F. Cleri, G. D'Agostino, V. Rosato, and M. Volpe, in *Nanotubes and Related Materials*, MRS Symposia Proceedings No. 633 (Materials Research Society, Pittsburgh, 2001), p. F14.8.1.
[28] N. Lehto and S. Oberg, Phys. Rev. Lett. **80**, 5568 (1998).
[29] X. Blase, K. Lin, A. Canning, S. G. Louie, and D. C. Chrzan, Phys. Rev. Lett. **84**, 5780 (2000).
[30] K. Lin and D. C. Chrzan, Comput. Model. Eng. Sci. **3**, 201 (2002).
[31] W. Cai, V. V. Bulatob, J. Chang, J. Li, and S. Yip, Philos. Mag. **83**, 539 (2003).
[32] M. S. Daw, Comput. Mater. Sci. **38**, 293 (2006).
[33] E. Ertekin, M. S. Daw, and D. C. Chrzan, Philos. Mag. Lett. **88**, 159 (2008).
[34] H. S. Seung and D. R. Nelson, Phys. Rev. A **38**, 1005 (1988).
[35] Z. Li, P. Dharap, P. Sharma, S. Nagarajaiaj, and B. I. Yakobson, J. Appl. Phys. **97**, 074303 (2005).
[36] G. Kresse and J. Fürthmuller, Phys. Rev. B **54**, 11169 (1996).
[37] G. Kresse and J. Fürthmuller, Comput. Mater. Sci. **6**, 15 (1996).
[38] D. Vanderbilt, Phys. Rev. B **32**, 8412 (1985).
[39] *Theory of Dislocations*, 2nd ed., edited by J. P. Hirth and J. Lothe (Krieger, Malabar, 1982).
[40] J. E. Marsden and T. J. R. Hughes, *Mathematical Foundations of Elasticity* (Prentice-Hall, Englewood Cliffs, 1983).
[41] T. Frankel, *The Geometry of Physics: An Introduction* (Cambridge University Press, Cambridge, 2001).
[42] W. Helfrich, Z. Naturforsch. C **28C**, 693 (1973).
[43] M. Hayashi, Phys. Lett. A **342**, 237 (2005).
[44] S. T. Hyde and M. O'Keeffe, Philos. Trans. R. Soc. London, Ser. A **354**, 1999 (1996).
[45] M. Arroyo and T. Belytschko, J. Mech. Phys. Solids **50**, 1941 (2002).